Volumetric Lidar Scanning of Wind Turbine Wakes under Convective and Neutral Atmospheric Stability Regimes

GIACOMO VALERIO IUNGO AND FERNANDO PORTÉ-AGEL

Wind Engineering and Renewable Energy Laboratory, École Polytechnique Fédérale de Lausanne, Lausanne, Switzerland

(Manuscript received 3 December 2013, in final form 24 June 2014)

ABSTRACT

Optimization of a wind farm's layout is a strategic task to reduce wake effects on downstream turbines, thus maximizing wind power harvesting. However, downstream evolution and recovery of each wind turbine wake are strongly affected by the characteristics of the incoming atmospheric boundary layer (ABL) flow, such as the vertical profiles of the mean wind velocity and the turbulence intensity, which are in turn affected by the ABL thermal stability. Therefore, the characterization of the variability of wind turbine wakes under different ABL stability regimes becomes fundamental to better predict wind power harvesting and to improve wind farm efficiency. To this aim, wind velocity measurements of the wake produced by a 2-MW Enercon E-70 wind turbine were performed with three scanning Doppler wind lidars. One lidar was devoted to the characterization of the incoming wind—in particular, wind velocity, shear, and turbulence intensity at the height of the rotor disc. The other two lidars performed volumetric scans of the wind turbine wake under different atmospheric conditions. Through the evaluation of the minimum wake velocity deficit as a function of the downstream distance, it is shown that the ABL stability regime has a significant effect on the wake evolution; in particular, the wake recovers faster under convective conditions. This result suggests that atmospheric inflow conditions, and particularly thermal stability, should be considered for improved wake models and predictions of wind power harvesting.

1. Introduction

The amount of wind turbines installed worldwide is growing rapidly, as wind energy is becoming one of the most popular renewable energy sources. Wind turbines are typically installed in clusters, denoted as wind farms, which are characterized by different layouts. For large wind farms, wind turbine wake interaction is becoming a crucial limitation for the growth rate of wind farm productivity with an increasing number of installed turbines (Wiser and Bollinger 2012). Turbine wakes develop as a consequence of the extraction of mean kinetic energy from the wind, and its conversion by the turbines into torque and, in turn, into electricity. The sudden reduction of kinetic energy at the turbine rotor location leads to the formation of a turbulent wake flow, which is characterized by a strong wind velocity deficit and an enhanced turbulence level with respect to the incoming wind.

When a wind farm is designed with a relatively small streamwise spacing between turbines, it is known that waked turbines will experience a significant decrease of the power production, because of the reduced wind velocity of the incoming wake flow, and also an increase of the fatigue loads connected to the higher wake turbulence level. In Barthelmie et al. (2010), statistical analysis of the power production of two large offshore wind farms with different turbine spacings—10.5 and 7 rotor diameters d—is reported. In that study, for turbine columns aligned with the mean wind direction, reduction of the power production for the downstream turbines was up to 40% compared with the power produced by the turbines deployed in the first row of the wind farm.

The structure and evolution of wind turbine wakes and their mutual interactions within a wind farm are affected by the flow characteristics of the atmospheric boundary layer (ABL). Indeed, wind turbines are immersed in a region of the ABL characterized by different levels of shear, stratification, and turbulence, which vary on daily and seasonal cycles (Larsen et al. 2007). Wind characteristics change with the stability regime of

Corresponding author address: F. Porté-Agel, Wind Engineering and Renewable Energy Laboratory, École Polytechnique Fédérale de Lausanne, GR B2 391, Station 2, CH-1015 Lausanne, Switzerland.
E-mail: fernando.porte-agel@epfl.ch

DOI: 10.1175/JTECH-D-13-00252.1

the ABL, which can be classified as stable, neutral, and convective. A convective ABL is typically observed onshore during daytime, when the terrain is heated by the sun. Under ABL convective conditions, heat transfer between the terrain and the air produces positive buoyancy, which leads to increased turbulence levels (Stull 1988). On the other hand, a stable ABL is typically observed during nighttime, and it is characterized by reduced turbulence levels and a significant wind shear. Finally, a neutral ABL represents a transitional regime between convective and stable regimes, and vice versa. For a neutral ABL, the mean potential temperature gradient is negligible and turbulence is mainly produced by shear in proximity of the terrain. Several studies have shown that ABL stability can affect noticeably power harvesting (Elliott and Cadogan 1990; Motta et al. 2005; Sumner and Masson 2006; Gottschall and Peinke 2008). In van der Berg (2008), investigations of full-scale turbines show a larger power harvesting under stable ABL conditions compared with neutral conditions. This result is in agreement with the work presented in Wharton and Lundquist (2010), which reports a lower power production from a single turbine operating in a convective ABL compared with stable conditions. Regarding the effects of ABL stability on the downstream evolution of wind turbine wakes, in Baker and Walker (1984) wake measurements performed with kite anemometry behind a 2.5-MW wind turbine showed a slower wake recovery for stable regimes, characterized by relatively lower turbulence levels. Recently, wind tunnel tests of downscaled wind turbine models immersed in a convective or neutral ABL were presented in Zhang et al. (2013). It was found that the enhanced turbulence, associated with positive buoyancy under convective conditions, leads to a larger flow entrainment and, thus, a faster wake recovery rate.

The characterization of the wake flow produced by real wind turbines represents a challenging task because of the large volume covered by the wake, which can also move because of the varying turbine yaw angle. Regarding the measurement techniques used for wind energy research, a remarkable improvement has been achieved through the introduction of the Doppler wind lidar technique. Doppler wind lidars are laser-based instruments that allow the measurement of the wind velocity component in the laser beam direction, which is denoted as radial velocity or line-of-sight (LOS) velocity. This remote sensing technique consists of the emission of a laser beam into the atmosphere, which is backscattered because of the presence of aerosol in the ABL. The radial wind velocity is then measured through the evaluation of the Doppler frequency shift on the backscattered laser beam. More details about lidar measurement techniques for the characterization of wind turbine wakes can be found in Iungo and Porté-Agel (2013).

Regarding lidar measurements for wind energy research, several studies have been published over the last few years. Nacelle-mounted lidar tests of wind turbine wakes were performed in Bingöl et al. (2010) and Trujillo et al. (2011), whereas ground-based lidar measurements were performed in Käsler et al. (2010), Iungo and Porté-Agel (2013), Iungo et al. (2013b), and Aitken et al. (2014). Vertical velocity profiles of the incoming wind and of the wind turbine wake flow were simultaneously carried out through two wind profile lidars by Rhodes and Lundquist (2013). Wake velocity deficit and wake turbulence were characterized through fixed location measurements, thus by analyzing a small range of wind directions corresponding to one lidar roughly positioned at the transversal middle location of the wake. In that study, the wind profile lidars had a relatively coarse spatial resolution, characterized by sampling volumes of height equal to $0.24d$, and by circular horizontal cross sections with diameters of $0.67d$, $1.25d$, and $1.83d$ at the wind turbine bottom-tip height, hub height, and top-tip height, respectively. Therefore, these relatively large sampling volumes are expected to lead to a substantial spatial averaging, and, thus, smoothing of the measured mean velocity and turbulence intensity profiles.

A scanning Doppler wind lidar was used in Smalikho et al. (2013) to perform conical scans of the wake produced by a 2.3-MW wind turbine. These authors found that the downstream extent of the wake was halved (from 680 to 340 m) for an increased turbulent energy dissipation rate (from 0.0066 to 0.013 $m^2 s^{-3}$). For the present campaign, measurements of the turbulent kinetic energy dissipation rate were not performed; thus, a direct comparison with the mentioned work has not been performed.

In this paper, wind lidar measurements of the wake produced by an Enercon E-70 2-MW wind turbine under different atmospheric conditions are presented. Wake measurements were performed simultaneously with three scanning Doppler wind lidars. One lidar was devoted to the characterization of the incoming wind over the rotor disc, while the other two lidars performed wind velocity measurements of the wind turbine wake through volumetric scans. The characteristics of the incoming wind were also monitored with a sonic anemometer installed on a 3-m tripod, which was located in proximity of the wind turbine.

The variability in the downstream evolution of the wind turbine wake is analyzed for different ABL conditions, and in particular for convective and neutral ABL stability regimes. The wake velocity deficit is evaluated as a function of the downstream location and

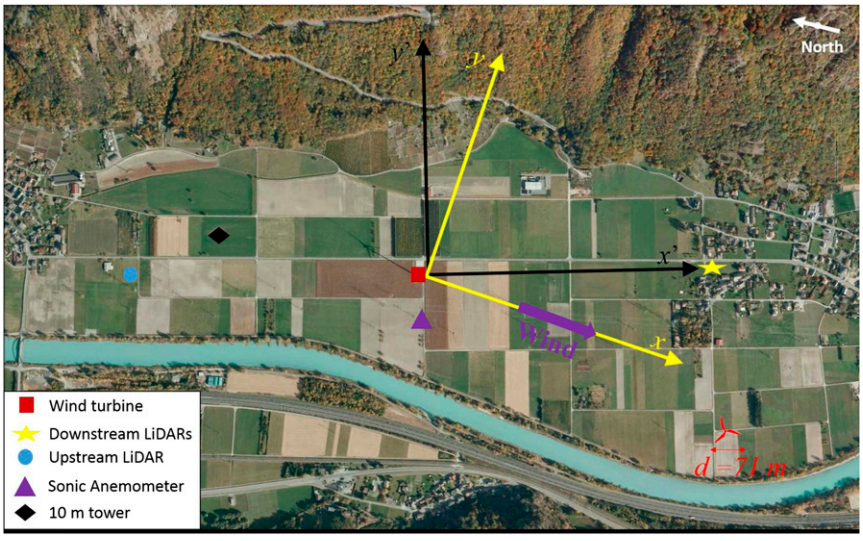

FIG. 1. Map of the site with wind turbine and instrument locations indicated by symbols described in the legend.

then fitted through a power law, whose exponent is considered to be a good parameter for the evaluation of the recovery rate of the wake velocity deficit. The paper is organized as follows: the tested wind turbine, the site, and the used lidars are described in section 2. Measurements for the characterization of the incoming wind field and ABL stability are then reported in section 3. Volumetric scans of the wind turbine wake and analysis of the wake recovery under different ABL stability regimes are provided in section 4. Finally, conclusions are drawn in section 5.

2. Wind turbine site and experimental setup

The field campaign was carried out during the period between June and October 2012. The tested wind turbine is an Enercon E-70, with a rotor diameter d of 71 m and a hub height H of 98 m. The rotor is connected to an Enercon direct-drive annular generator and it is characterized by a maximum capacity of 2.3 MW. The turbine has a gearless system with variable speed and active pitch control. The rotor consists of three blades made of glass-reinforced plastic (GRP; epoxy resin) and provides integrated lightning protection. The rotational frequency of the rotor can vary from 0.1 up to 0.36 Hz. The cut-in wind velocity is 2.5 m s^{-1}, whereas the cut-out velocity is 34 m s^{-1}.

This wind turbine is located in Collonges, Switzerland, within a relatively narrow flat valley bottom about 1 km wide in the Valais region, and it is surrounded by mountains with heights around 2500 m. Thus, the topography plays a strong role in the wind characteristics. The wind direction with the highest incidence is at 340° from the north, which typically occurs during afternoons. It is a thermal wind blowing from the warmer area of the Lake Geneva toward the Alps and is mainly canalized in the valley. The other typical wind has roughly the opposite direction, that is, 160° SSE from the north; it typically blows early in the morning and is commonly slightly stronger than the northerly wind. A map of the site and experimental setup is reported in Fig. 1.

Wind velocity measurements were performed simultaneously with three Stream Line wind lidars, produced by Halo Photonics. These lidars emit wave trains with a wavelength of 1.5 μm at a frequency of 15 kHz. They are of the scanning type; that is, the laser beam direction is fully controlled by the user by setting different values of the azimuth and elevation angles of the laser beam. The highest spatial resolution of the Stream Line lidar is 18 m; that is, velocity measurements can be acquired at points evenly spaced along the laser beam with a distance of 18 m. The first available measurement point is at a distance of 45 m from the lidar location and the maximum range is about 3 km. The maximum sampling frequency is 0.77 Hz. The main specifications of the Stream Line lidar are summarized in Table 1. Lidar measurements were performed by using one laser ray for each tested direction. Indeed, a good accuracy on the evaluation of the radial velocity was generally achieved because of wake wind turbulence and the increased aerosol concentration within the wake, which is due to the lower pressure promoting flow entrainment into the wake. The accuracy of the used lidars in the measurement of the radial velocity was previously assessed

TABLE 1. Specifications of the Stream Line lidar produced by Halo Photonics. Full width at half maximum (FWHM).

Wavelength	1.5 μm
FWHM pulse duration	150 ns
Repetition rate	15 kHz
Frequency bandwidth	50 MHz
Telescope aperture	50 mm
Measurement range	45 m up to 2 km
Length of the lidar range gate	18 m
Focus range	300 m up to infinity
Maximum sampling rate	0.77 Hz

against sonic anemometer data, and it is about 0.5% (Carbajo-Fuertes et al. 2014).

The ABL stability is characterized through the evaluation of the Obukhov length L, which requires single-point heat flux measurements in the surface layer. These measurements were performed with a Campbell Scientific CSAT3 sonic anemometer, which was installed on a tripod at a height of 3 m in the proximity of the turbine location. Specifically, it was placed at a transversal distance of about 100 m in order to avoid any effect of the wind turbine on the measurements (see Fig. 1). Wind velocity and temperature data were acquired with a sampling frequency of 20 Hz during the entire testing period.

The wind turbine location and the chosen lidar locations were determined through a GPS system. Moreover, azimuthal displacements of the lidar laser beam, needed to reach the measurement targets, were also evaluated through the GPS. The used GPS is the GRS-1 by Topcon Positioning Systems, which works with GPS and Globalnaya navigatsionnaya sputnikovaya sistema (GLONASS; otherwise called Global Navigation Satellite System) receivers. This GPS can achieve a precision of 300 mm with the Differential GPS (DGPS) network.

A reference frame used for this field campaign has its origin at the base of the wind turbine tower. The x axis corresponds to the mean wind direction, positive in the downstream direction. The mean wind direction was evaluated for the three different types of periods considered in the analysis: the sampling period of each volumetric scan, 5-min periods, and 10-min periods. The z axis is along the vertical direction, positive upward, while y axis is along the spanwise direction, oriented in a way to produce a right-handed Cartesian coordinate system. A supplementary reference frame was used for the postprocessing of the lidar data; its x' axis corresponds to the line connecting the turbine location and the lidars deployed downstream of the turbine, the z axis is unchanged, and the y' axis is along the spanwise direction, oriented in a way to produce a right-handed Cartesian coordinate system. The two used reference frames are reported in Fig. 1. More details about the experimental setup and the tested wind turbine can be found in Iungo et al. (2013b).

3. Characterization of the incoming wind field and ABL stability

The incoming wind conditions were continuously monitored through one wind lidar located at a distance of $12d$ upwind of the wind turbine location. This lidar performed different scan types: staring over fixed directions, plan position indicator (PPI) scans sweeping the laser azimuthal angle while keeping fixed its elevation angle, and range–height indicator (RHI) scans sweeping the laser elevation angle while keeping fixed its azimuthal angle [for details about the different scanning techniques see, e.g., Iungo and Porté-Agel (2013)]. PPI and RHI scans were performed in order to evaluate the wind heterogeneity of the ABL in the horizontal and vertical directions, respectively. Moreover, staring measurements were continuously performed by setting the azimuthal angle of the lidar laser beam in the mean wind direction. The latter was evaluated through lidar vertical wind profiles and PPI scans. PPI scans were typically performed every 15 min and each PPI scan had a sampling period of 40 s. Wind conditions were also monitored through a cup anemometer and wind vane installed on a 10-m tower deployed in proximity of this lidar (see Fig. 1).

Staring measurements were performed by setting the lidar elevation angle at 7.8° in order to reach the turbine hub height at a distance of $2d$ upwind of the turbine location. This location was used to evaluate the reference wind velocity at hub height U_{hub}. By assuming that the azimuthal angle of the lidar laser beam is perfectly aligned with the mean wind direction, a good approximation of the horizontal velocity is simply obtained by considering that the lidar radial velocity is the projection of the horizontal velocity over the laser beam direction. The lidar staring measurements were carried out with the maximum sampling frequency of 0.77 Hz in order to characterize not only the evolution of the mean wind velocity but also wind velocity fluctuations (Iungo et al. 2013b; Iungo and Porté-Agel 2013; Carbajo-Fuertes et al. 2014).

Vertical profiles of the mean velocity of the incoming wind were characterized with the dimensionless wind shear exponent α through the following power law:

$$U(z) = U_R\left(\frac{z}{z_R}\right)^{\alpha}, \tag{1}$$

where $U(z)$ is the mean horizontal wind speed measured at height z, while U_R is a reference velocity measured at

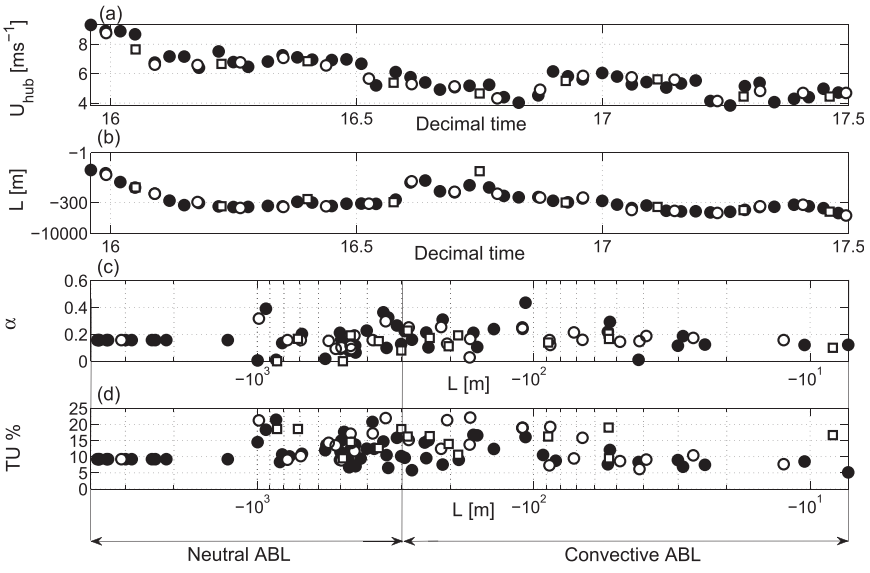

FIG. 2. Characterization of the incoming wind: (a) hub height velocity U_{hub}; (b) surface layer Obukhov length L; (c) dimensionless wind shear exponent α; and (d) wind turbulence intensity at hub height TU. [Symbols represent statistics performed over different time periods: filled circles (•) show the single volumetric scan (110 s); an open circle (○), 5 min; and the open square (□), 10 min.]

a height typically very close to the ground, z_R (see, e.g., Smith et al. 2013). The fitting of the wind measurements was performed by considering heights within the range $-1 < (z - H)/d < 1$. A stable ABL regime is typically characterized by the presence of a significantly sheared flow, which is generally associated with $\alpha > 0.2$. Conversely, a convective ABL regime is characterized by relatively uniform wind velocities along the vertical direction, thus $\alpha < 0.1$. Finally, a neutral ABL regime is characterized by $0.1 < \alpha < 0.2$ (Rareshide et al. 2009; Wharton and Lundquist 2012; Smith et al. 2013).

The ABL stability was characterized through the evaluation of the Obukhov length L, which is an indicator of atmospheric mixing conditions in the surface layer following the Monin–Obukhov similarity theory (Monin and Obukhov 1954; Obukhov 1971; Nieuwstadt 1984; Stull 1988). The Obukhov length is proportional to the height above the surface where buoyancy-produced turbulence begins to dominate over shear-produced turbulence. It is calculated as follows:

$$L = -\frac{\theta_v u_*^3}{kg\overline{w'\theta_v'}}, \tag{2}$$

where θ_v is the virtual potential temperature (kelvins), k is the von Kármán constant (0.4), g is the gravitational acceleration, $\overline{w'\theta_v'}$ is the surface heat flux, and u_* is the friction velocity calculated as $u_* = (\overline{u'v'}^2 + \overline{v'w'}^2)^{1/4}$. Negative values of L are obtained for convective (statically unstable) ABL regimes, whereas positive L values correspond to stable ABL regimes. For practical applications, the ABL is often considered stable for $0\,\text{m} < L < 200\,\text{m}$, whereas it is convective for $-300\,\text{m} < L < 0\,\text{m}$ (see, e.g., Wharton and Lundquist 2010). Outside of those intervals—that is, $L < -300\,\text{m}$ or $L > 200\,\text{m}$—the ABL is considered neutral. For this site, during the testing period a transition from neutral to convective conditions was typically observed around 1000 local standard time (LST), while a transition from convective to neutral ABL regimes occurred at around 1700 LST. Unfortunately, a stable ABL was never observed during the testing period.

For this study, measurements carried out on 8 October 2012 are considered. That day was generally sunny, and a transition between the convective and neutral ABL regimes was observed 2 times during the afternoon. For the characterization of the incoming wind, statistics were performed over different types of time periods. In particular, key flow parameters were calculated for each volumetric scan (i.e., for a time period of 110 s), as well as over 5-min and 10-min periods, and the results are reported in Fig. 2. Statistics were also calculated for time periods of 20 min, but those results are not reported here because they were found to differ by less than 2% with respect to the corresponding values obtained by using 10-min periods. For the total duration of the measurements considered here, the mean incoming wind velocity at hub height U_{hub} evolved from 9 to 4 m s^{-1}

TABLE 2. Statistics of the incoming wind for different ABL stability regimes. (left) Dimensionless wind shear exponent α. (right) Turbulence intensity at hub height TU.

Dimensionless wind shear exponent α			Turbulence intensity at hub height TU		
	Convective ABL	Neutral ABL		Convective ABL (%)	Neutral ABL (%)
Mean	0.14	0.16	Mean	10.3	9.4
Median	0.13	0.17	Median	9.3	9.7
Max	0.44	0.39	Max	22	21.5
Min	0.01	0.01	Min	5.1	6.5
Std dev	0.13	0.13	Std dev	3.4	3.6

(Fig. 2a). The mean wind velocity was also evaluated over the whole rotor disk, that is, for the range $-0.5 < (z - H)/d < 0.5$; however, the maximum difference between the latter and U_{hub} was about 4%, indicating a negligible effect of the wind shear on the definition of a reference wind velocity for the considered testing period.

The Obukhov length L reported in Fig. 2b clearly highlights that for the chosen testing period, the ABL was convective around 16 h LST and a transition to neutral occurred around 16.2 h LST (decimal time) because of an overcast. Then, the ABL turned back to convective at 16.6 h LST, and became finally neutral around 17 h LST, because of the reduced solar radiation in the late afternoon.

Besides the mean wind velocity, the incoming wind is also characterized through the evaluation of the dimensionless shear exponentα, defined in Eq. (1), and the turbulence intensity, which are plotted in Figs. 2c and 2d, respectively, while their statistics are reported in Table 2. For the tests performed during an ABL convective regime—that is, with $-300\,\text{m} < L < 0\,\text{m}$—$\alpha$ had a noticeable variability and a mean value of 0.14. A similar mean α value (0.16) was observed for the neutral ABL regime. Regarding wind turbulence intensity at hub height (TU), which is equal to the ratio between standard deviation and mean value of the velocity as a percentage, a mean value of 10.3% was obtained for ABL convective conditions, whereas 9.4% was found for neutral conditions. The above-mentioned results indicate that wind shear and turbulence intensity of the incoming wind at the turbine hub height are only weakly influenced by ABL stability. This feature makes this test site suitable for investigations of the variability of wind turbine wakes due to the ABL thermal stability. Indeed, similar wind turbulence intensity and wind shear are observed for different ABL stability regimes. However, the analysis of the sonic anemometer data, which were needed for the characterization of the ABL stability and wind turbulence within the ABL surface layer, clearly shows a significant effect of atmospheric stability on wind turbulence. Indeed, in Fig. 3a the ratio between the standard deviation of the horizontal velocity σ_U and the friction velocity u_*, which represents wind turbulence intensity within the surface layer, is reported as a function of the ratio between the ABL height z_i and the Obukhov length L. For convective regimes, the parameter $\sigma_U u_*^{-1}$ decreases with reducing L. In particular it is roughly proportional to $(-z_i L^{-1})^{1/3}$ as found in Panofsky et al. (1977) for a free convective flow (for the experimental data, a best-fit exponent of 0.36 with an R^2 value of 0.96 was estimated). Approaching the transition from convective to neutral regime, $\sigma_U u_*^{-1}$ reaches roughly an asymptotic value equal to 2, which is in good agreement with previous field measurements and large-eddy simulations (LES; see, e.g., Takeuchi 1961; Basu et al. 2006). A similar behavior is also observed for the vertical velocity, with $\sigma_W u_*^{-1}$ being proportional to $(-zL^{-1})^{1/3}$ in the convective regime, as previously reported by Kaimal et al. (1982) (for the experimental data, a best-fit exponent of 0.37 with an R^2 value of 0.96 was estimated). Then, approaching the transition from convective to neutral ABL, $\sigma_W u_*^{-1}$ reaches an asymptotic value of about 1, which is again in agreement with

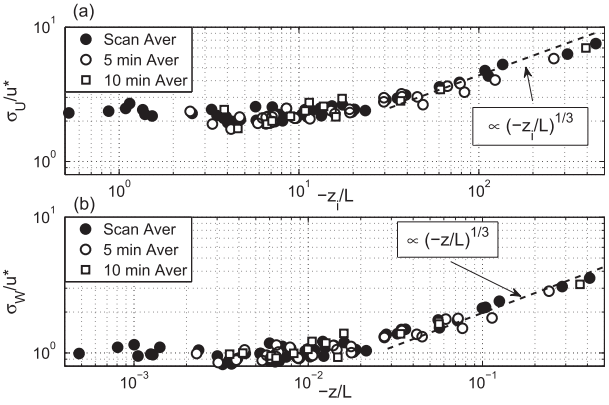

FIG. 3. Characterization of the incoming wind through sonic anemometer data: (a) ratio between the standard deviation of the horizontal velocity σ_U and the friction velocity u_*; (b) ratio between the standard deviation of the vertical velocity σ_W and the friction velocity u_*. [Symbols represent statistics performed over different time periods: filled circles (•) show the single volumetric scan (110 s); an open circle (○), 5 min; and the open square (□), 10 min.]

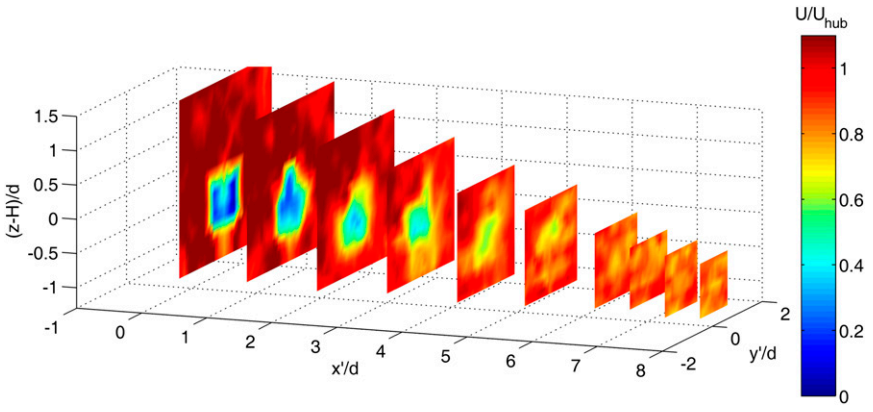

FIG. 4. Velocity field obtained through a volumetric scan (decimal time 16.7377). Transversal planes at different downstream locations (x/d = 0.6; 1; 2; 3; 4; 5; 6; 7.6; 8).

the results presented in Takeuchi (1961) and Basu et al. (2006). Therefore, within the ABL surface layer, a significant reduction of wind turbulence is observed as the ABL flow moves from convective to neutral. A similar reduction is also detected in the turbulent kinetic energy, shear stresses, and heat flux (not reported here for the sake of brevity). However, the same effect of atmospheric stability is not observed in the turbulence intensity measured at hub height using the lidar measurements (see Fig. 2d). This result indicates that the incoming wind at the rotor height is above the surface layer, and it is likely to be influenced by the steep topography that surrounds the flat valley bottom, where the turbine is placed.

Summarizing, the similar turbulence intensity and wind shear observed at hub height for different ABL stability regimes, the flat homogeneous bottom of the valley, and the remarkable effect of the ABL stability on the wind turbulence within the ABL surface layer make this test site suitable for investigations on the variability of wind turbine wakes under different ABL stability regimes. Indeed, the observed variability of the wake recovery is mainly the result of the wake flow on different heat flux and turbulent stresses in the surface layer, resulting from different stability regimes.

4. Volumetric scans of the wind turbine wake

As mentioned in section 1, a wind lidar is only sensitive to the wind velocity component parallel to the emitted laser beam; thus, 1D velocity profiles can be obtained by staring the laser beam over a fixed direction. However, measurement techniques with different levels of complexity can be designed in order to measure 2D and 3D velocity fields, which imply different sampling periods and measurement volumes (Newsom et al. 2005; Chan and Shao 2007; Emeis et al. 2007; Xia et al. 2008; Lin et al. 2008; Kongara et al. 2012; Iungo and Porté-Agel 2013).

For measurements of wind turbine wakes, a technical issue is represented by the variability of the wind direction and turbine yaw angle, which could generate misleading physical interpretations of the acquired wind data. Indeed, the relative position between the measurement points and the actual wake location can be unknown or incorrect. Thus, to overcome this possible error source, the whole wake velocity field was measured through volumetric scans. These measurements were carried out by varying both elevation and azimuthal angles of the lidar laser beam—in particular, the azimuthal angle within a range of 20°, centered with the wind turbine hub and with angular steps of 2°, while the elevation angle was varied from 2° up to 16° with an angular step of 2°. To reduce the sampling period required for each volumetric scan, one lidar measured by varying the elevation angle from 2° up to 8°, while the other one from 10° up to 16°. Thus, each lidar measured over half-tested volume. With this procedure a sampling period of 110 s per scan was obtained. The two lidars were triggered on the start of each volumetric scan, even though they were not perfectly synchronized on each displacement of the laser beam. After a complete volumetric scan, a maximum delay between the two lidars of about 0.3 s was estimated, which is negligible compared to the 110 s needed for a whole volumetric scan. Then, the lidars started simultaneously the following scan.

A typical wake velocity field measured through a volumetric scan is reported in Fig. 4. For these tests the two lidars were deployed at the downstream location x'/d = 12. A noticeable error in the evaluation of the radial velocity can be made for downstream distances $x/d <$ 0.5, because of wind turbine reflections of the laser

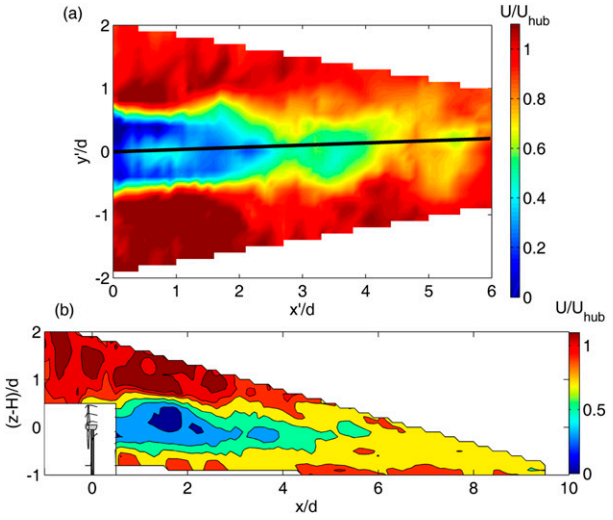

FIG. 5. Velocity field obtained through a volumetric scan (decimal time 16.7377): (a) over the horizontal plane at hub height (vertical symmetry plane of the wake highlighted with a black line) and (b) over the wake vertical symmetry plane.

beam. Therefore, those data were not considered in the present study. To analyze the wind velocity field, all the acquired radial velocities were extrapolated on the nodes of a structured mesh with a spatial resolution of $0.2d$ through a 3D Delaunay triangulation (Delaunay 1934). In Fig. 4 transversal planes are reported for different downstream locations ($x'/d = 0.6, 1, 2, 3, 4, 5, 6, 7, 7.6, 8$), which allow the characterization of the wind turbine wake over different cross sections. In particular, wake morphology can be clearly observed with its location and wake velocity deficit.

The evaluation of the velocity field over the horizontal plane located at hub height, which is reported in Fig. 5a, allows a more detailed characterization of the wake recovery. Indeed, this figure shows that the strong velocity deficit observed in the near-wake region gradually recovers, moving downstream, while a slight increase of the wake width is also observed, especially for distances $x/d > 3$. It is important to point out that the measurements obtained through a volumetric scan and extrapolated over the horizontal plane at hub height allow for overcoming a typical issue connected to PPI scans where, although a description of the wake recovery is provided, the obtained data are collected over an inclined conical surface and not exactly at hub height.

In Fig. 5a the wake vertical symmetry plane, which is the vertical plane passing through the turbine location and parallel to the mean wind direction, is represented with a black line. For the considered test it is rotated 2° counterclockwise from the x' axis. Subsequently, the wind velocity field is also evaluated over the wake vertical symmetry plane, as reported in Fig. 5b, showing the wake velocity deficit and the wake recovery. These wind velocity data are analogous to the ones achievable through an RHI scan, but avoiding the risk of a misalignment between the RHI measuring plane and the actual wake vertical symmetry plane.

Through the detection of the wake vertical symmetry plane, a new reference frame can be defined by rotating the existing one around the z axis in order to obtain the x–z plane coincident with the wake vertical symmetry plane. The velocity field evaluated for the new reference frame is characterized by only one nonnegligible component, which is the one oriented along the x axis and referred to as axial velocity. This is a reliable assumption for wind turbine wake flows, except for the very near wake ($x/d < 1$), where a small transversal velocity component could be present due to wake swirl (Iungo et al. 2013a,b; Viola et al. 2014). Therefore, for each scan an approximated axial velocity is evaluated by considering that the radial velocity is the projection of the axial velocity over the respective lidar laser beam direction (Machefaux et al. 2012; Iungo and Porté-Agel 2013).

Averaged velocity fields were also calculated from several volumetric scans in order to characterize the wake recovery over longer sampling periods. This procedure allows the enhancement of the statistical stationarity of the parameters evaluated for the characterization of the wake recovery and to produce statistics comparable to the ones typically obtained through numerical simulations and wind tunnel tests (see, e.g., Porté-Agel et al. 2011; Wu and Porté-Agel 2011; Iungo et al. 2013a; Viola et al. 2014). Generally, the mean radial velocity field was calculated from three consecutive scans, thus for a sampling period of 330 s, with the constraints of a maximum difference between the three considered scans of 1 m s^{-1} for U_{hub} and 2° for the mean wind direction. An example of the above-mentioned procedure is presented in Fig. 6. Specifically, horizontal cross sections of the radial velocity field at hub height are reported for three consecutive volumetric scans, together with their averaged velocity field.

Next, the wake velocity deficit and its downstream recovery are analyzed with two different methods—that is, by selecting for each downwind distance the minimum value of the axial velocity over a transversal plane, and over its intersection with the wake vertical symmetry plane. A typical downstream evolution of the wake velocity deficit is shown in Fig. 7; it is evident that the two criteria are in good agreement for the evaluation of the wake velocity deficit.

In several works—for example, Crespo and Hernández (1986), Luken et al. (1986), Högstrom et al. (1988), Magnusson and Smedman (1996, 1999), Vermeer et al. (2003), and Zhang et al. (2013)—the downstream

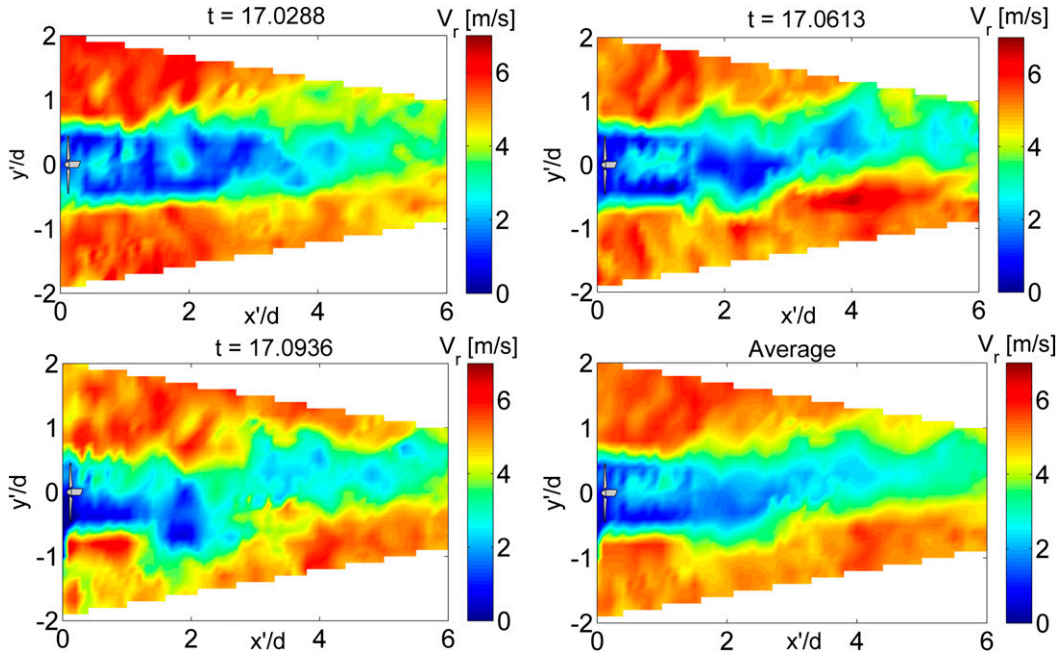

FIG. 6. Averaging of the wind velocity field of three consecutive volumetric scans. Horizontal cross sections at hub height.

recovery of the wake velocity deficit is typically represented by the following power law:

$$\frac{U_{\text{hub}} - U_{\text{min}}}{U_{\text{hub}}} = A\left(\frac{x}{d}\right)^{n}, \tag{3}$$

where U_{hub} is the reference velocity, which is measured by the lidar located upwind for the characterization of the incoming wind. This reference velocity is also assessed through a comparison with the velocity measured by the two downwind lidars and averaged among the points located at hub height in the region $-1 < x/d < 1$, for transversal locations $-2 < y/d < -1$ and $1 < y/d < 2$—that is, on both sides of the rotor. Differences typically lower than 2% are obtained for the two different measurements. Term U_{min} is the minimum axial velocity observed at a certain downstream location. The parameter A depends on the turbine characteristics and is related to the thrust coefficient, while the exponent n is connected to the rate of wake recovery; a larger n corresponds to a slower wake recovery. From the above-mentioned works, typical values for these coefficients are $A \in [1, 3]$ and $n \in [-1.25, -0.25]$. In Fig. 7 the fitting curve corresponding to the considered volumetric scan is reported with a solid black line, which shows that the recovery of the wake velocity deficit can be adequately represented through the law reported in Eq. (3) (R^2 value of the fit equal to 0.89). However, some scattering

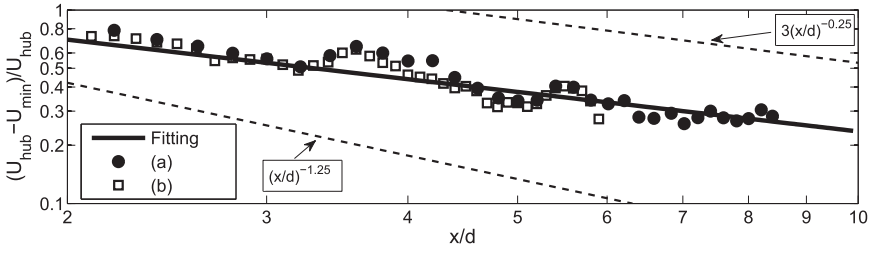

FIG. 7. Velocity field obtained through a volumetric scan: velocity deficit as a function of the downstream location evaluated through two methods: (a) as minimum of the axial velocity for the different transversal planes, filled circles (•); and (b) as minimum of the axial velocity over the wake vertical symmetry plane for different downstream locations, empty squares (□). The solid black line is the fitting curve of the wake velocity deficit as defined in Eq. (3). The two dashed black lines correspond to the extreme values of the parameters A and n in Eq. (3) reported in literature.

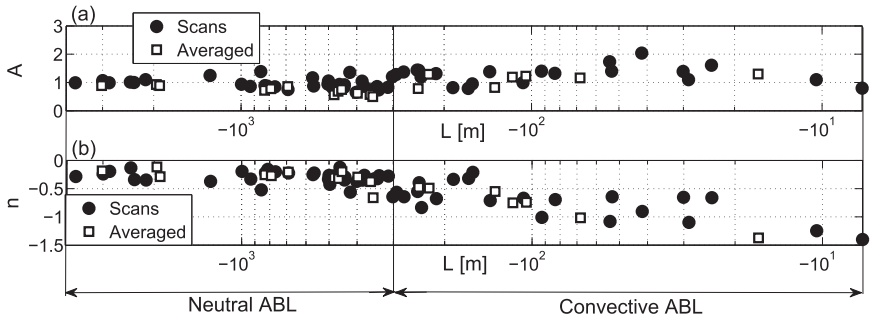

FIG. 8. Fitting coefficients of the wake velocity deficit function in Eq. (3) as a function of the Obukhov length L: (a) fitting coefficient A and (b) fitting coefficient n. [Symbols: parameters obtained from single volumetric scans are shown by filled circles (•); parameters obtained from averages of three consecutive volumetric scans are shown by empty boxes (□).

around the fitting curve is observed due to the turbulent nature of the wind turbine wake flow.

The fitting coefficients A and n were evaluated for each volumetric scan and also for the mean velocity fields obtained by averaging the wind data from three consecutive scans. Fitting coefficients A and n are reported in Fig. 8 as a function of the Obukhov length L, that is, of the ABL stability condition; moreover, their statistics are reported in Tables 3 and 4. For the convective ABL regime, the mean value of the coefficient A is 1.46 for the single scans and 1.03 for the averaged data, whereas for the neutral regime its mean value is 0.95 and 0.78 for the single and averaged scans, respectively. Considering that typical values for the coefficient A are included within the interval [1, 3], it appears that ABL stability has only a weak effect on the fitting coefficient A.

The downstream recovery of the wake velocity deficit is then characterized through the fitting coefficient n in Eq. (3). From Fig. 8b it is evident that n is generally increased (less negative) moving from a convective ABL stability regime to a neutral one. For the single scans, the mean value of n changes from −0.68 for the convective regime to −0.29 for the neutral one; analogously, for the averaged data, it varies from −0.76 to −0.26. Considering that typical values of n are included within the interval [−1.25, −0.25], it can be concluded that the influence of the ABL stability condition on the wake recovery is remarkable. Specifically, a faster wake recovery is observed for convective ABL regimes. This feature is largely appreciable in Fig. 9, where all the fitting curves of the downstream evolution of the wake velocity deficit evaluated for each volumetric scan are reported. The curves associated with a neutral ABL regime are reported in blue, whereas the ones ascribed to a convective ABL are reported in red. The latter have clearly a higher slope, which is due to a faster recovery of the wake velocity deficit. These results are in good agreement with the wind tunnel experiments performed by Zhang et al. (2013), for which a relatively faster wake recovery was also observed under convective conditions.

To investigate possible physical explanations for the variability of the wake recovery observed for different ABL stability regimes, the fitting coefficient n of Eq. (3) is also analyzed as a function of the wind velocity at hub height U_{hub}. The thrust coefficient of a wind turbine C_T is a function of the tip speed ratio, which is the ratio between the rotational velocity at the blade tip and U_{hub}. Consequently, U_{hub} could affect C_T, which is typically an input for different far-wake models in order to predict the wake velocity deficit and the growth of the wake width as a function of the downstream location

TABLE 3. Statistics of the fitting coefficient A of the wake velocity deficit function defined in Eq. (3), evaluated for different ABL stability conditions and different sampling periods. (left) Statistics of A calculated from each volumetric scan. (right) Statistics of A calculated from averaged velocity fields of three consecutive scans.

	Single volumetric scans			Averaged velocity fields	
	Convective ABL	Neutral ABL		Convective ABL	Neutral ABL
Mean	1.46	0.95	Mean	1.03	0.78
Median	1.38	0.92	Median	1.18	0.77
Max	2.1	1.38	Max	1.30	0.98
Min	0.78	0.65	Min	0.70	0.57
Std dev	0.62	0.17	Std dev	0.27	0.15

TABLE 4. Statistics of the fitting coefficient n of the wake velocity deficit function defined in Eq. (3), evaluated for different ABL stability conditions and different sampling periods. (left) Statistics of n calculated from each volumetric scan. (right) Statistics of n calculated from averaged velocity fields of three consecutive scans.

	Single volumetric scans			Averaged velocity fields	
	Convective ABL	Neutral ABL		Convective ABL	Neutral ABL
Mean	−0.68	−0.29	Mean	−0.76	−0.26
Median	−0.66	−0.28	Median	−0.70	−0.28
Max	−0.21	−0.12	Max	−0.48	−0.12
Min	−1.4	−0.64	Min	−1.37	−0.66
Std dev	0.27	0.1	Std dev	0.15	0.07

(see, e.g., Crespo et al. 1999; Vermeer et al. 2003; Bastankhah and Porté-Agel 2014). In Eq. (3) the influence of C_T on the wake velocity deficit is represented by the parameter A. In Fig. 10a no noticeable correlation between the fitting coefficients n and U_{hub} is observed, indicating that the observed variability in the wake recovery is not related to possible changes of the operational regime of the turbine. This result is in agreement with the negligible variability observed for the fitting coefficient A of Eq. (3) for different ABL stability regimes (see Fig. 8a).

Figure 10b shows the fitting coefficient n as a function of the ratio between the standard deviation of the horizontal velocity, σ_U and the friction velocity u_*. Considering that σ_U/u_* was computed from sonic anemometer measurements (collected at a height of 3 m), it can be considered as a good measure of the turbulence level in the surface layer. In Fig. 3a it has been shown that σ_U/u_* increases monotonically with increasing L, thus moving from neutral to convective ABL regimes. Here in Fig. 10b, it is shown that the fitting coefficient n decreases with increasing σ_U/u_*, which indicates that the enhanced turbulence intensity in the surface layer under convective conditions leads to a faster wake recovery compared to neutral conditions. Summarizing, the increased turbulence levels observed within the ABL surface layer under convective conditions are likely associated with an increased exchange of momentum and energy between the turbine wake and the surrounding ABL flow. This, in turn, leads to an enhanced flow entrainment within the wake and, thus, to a faster wake recovery.

5. Concluding remarks

A field campaign was performed in order to investigate the influence of atmospheric thermal stability on the downstream evolution and recovery of wind turbine wakes. To this aim velocity measurements were simultaneously carried out with three scanning Doppler wind lidars. One lidar was devoted to the characterization of the incoming wind—in particular, mean velocity at hub height, wind shear, and wind turbulence intensity. The thermal stability of the atmospheric boundary layer (ABL) was characterized through the evaluation of the Obukhov length, which was obtained from single-point heat flux measurements carried out with a sonic anemometer. It has been observed that characteristics of the

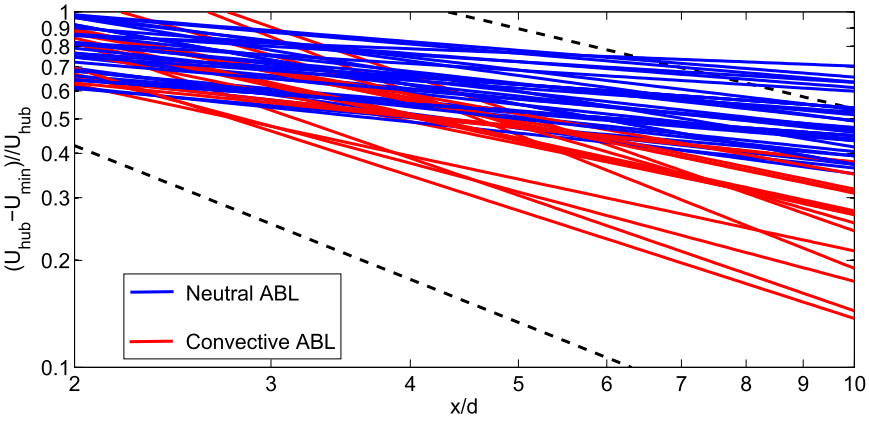

FIG. 9. Fitting curves of the wake velocity deficit as a function of the downstream location as defined in Eq. (3). Blue lines are associated with volumetric scans performed under neutral ABL conditions, whereas the red lines are obtained under convective conditions.

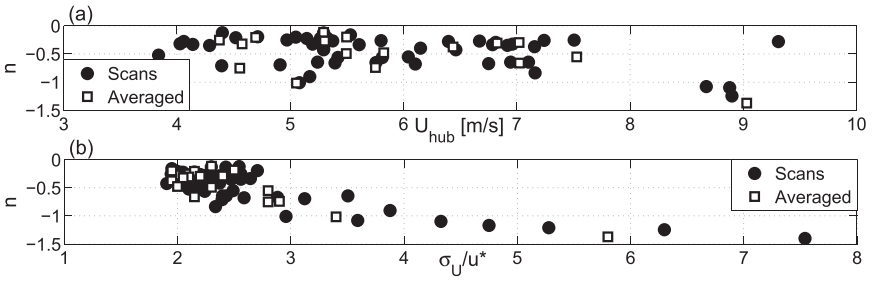

FIG. 10. Fitting coefficient n of the wake velocity deficit function in Eq. (3): (a) n as a function of the wind velocity at hub height U_{hub} and (b) n as a function of the ratio between the standard deviation of the horizontal velocity σ_U and the friction velocity u_* obtained from a sonic anemometer installed at 3-m height. [Symbols: filled circle (•) parameters obtained from single volumetric scans; empty square (□) parameters obtained from averages of three consecutive volumetric scans.]

incoming wind at hub height are not substantially affected by ABL stability because the rotor is above the surface layer, where the flow is mostly affected by the steep topography surrounding the valley where the wind turbine is located. However, a significant reduction of turbulence activity has been observed within the ABL surface layer moving from convective to neutral ABL regimes. These features make this test site suitable for investigations into the effects of ABL thermal stability on wind turbine wake recovery. Indeed, the observed wake variability is mainly the result of different heat flux and shear stresses in the surface layer, resulting from different ABL stability regimes.

The other two lidars performed volumetric scans of the wind turbine wake, which produced a very efficient measuring technique for the characterization of wind turbine wake flows. Measurements were carried out over the entire volume of the wake, in order to avoid any error on the evaluation of the relative position between measurement points and the actual location of the turbine wake. Moreover, the evaluation of the wind velocity field over the horizontal plane at hub height and over the vertical symmetry plane of the wake allows a detailed characterization of the downstream evolution and recovery of the wind turbine wake.

For the wake velocity fields obtained from each volumetric scan and from averages of three consecutive volumetric scans, the wake velocity deficit was evaluated as a function of the downstream location and then fitted through a power law. This analysis shows that the wind turbine wake recovers faster under convective conditions, compared with the neutral ones. This enhanced wake recovery rate is likely related to increased turbulence levels within the ABL surface layer, which promote ABL flow entrainment into the wake. A similar effect of ABL turbulence on the wake recovery has also been reported from previous wind tunnel tests (see Zhang et al. 2013) and large-eddy simulation studies (see Wu and Porté-Agel 2012).

This noticeable effect of ABL stability on the downstream evolution of wind turbine wakes should be definitely considered for improved wake models, which are essential for numerical simulations of wind turbine wake flows, and for prediction of wind power harvesting. A good comprehension of the variability of wind turbine wakes under different ABL regimes is also crucial for the evaluation of the environmental impact of wind turbine wakes on the local microclimate. Indeed, according to recent works, a different downstream extent of wind turbine wakes can modify the environmental footprint of wind farms (Zhou et al. 2012). However, longer testing periods and wind farm experiments are needed in order to obtain conclusive results on this topic. Overall, the wind turbine wake measurements presented herein provide a valuable dataset for the improvement and validation of numerical models (e.g., analytical models and large-eddy simulations) of wind turbine wakes.

Acknowledgments. This research was supported by the Swiss National Science Foundation (Grant 200021-132122) and the Swiss Federal Office of Energy. The authors are grateful to J. M. Rouiller (Comune de Lausanne), RhônEole, KholeNusbaumer SA, and SEIC-TELEDIS Groupe for their support in the preparation of the field campaign. Computing resources were provided by the Swiss National Supercomputing Centre.

REFERENCES

Aitken, M. L., R. M. Banta, Y. L. Pichugina, and J. K. Lundquist, 2014: Quantifying wind turbine wake characteristics from scanning remote sensor data. *J. Atmos. Oceanic Technol.,* **31,** 765–787, doi:10.1175/JTECH-D-13-00104.1.

Baker, R., and S. Walker, 1984: Wake measurements behind a large horizontal axis wind turbine generator. *Sol. Energy,* **33,** 5–12, doi:10.1016/0038-092X(84)90110-5.

Barthelmie, R. J., and Coauthors, 2010: Quantifying the impact of wind turbine wakes on power output at offshore wind farms. *J. Atmos. Oceanic Technol.,* **27,** 1302–1317, doi:10.1175/2010JTECHA1398.1.

Bastankhah, M., and F. Porté-Agel, 2014: A new analytical model for wind-turbine wakes. *Renewable Energy,* **70,** 116–123, doi:10.1016/j.renene.2014.01.002.

Basu, S., F. Porté-Agel, E. Foufoula-Georgiou, J.-F. Vinuesa, and M. Pahlow, 2006: Revisiting the local scaling hypothesis in stably stratified atmospheric boundary-layer turbulence: An integration of field and laboratory measurements with large-eddy simulations. *Bound.-Layer Meteor.,* **119,** 473–500, doi:10.1007/s10546-005-9036-2.

Bingöl, F., J. Mann, and G. C. Larsen, 2010: Light detection and ranging measurements of wake dynamics. Part I: One-dimensional scanning. *Wind Energy,* **13,** 51–61.

Carbajo-Fuertes, F., G. V. Iungo, and F. Porté-Agel, 2014: 3D turbulence measurements using three synchronous wind lidars: Validation against sonic anemometry. *J. Atmos. Oceanic Technol.,* **31,** 1549–1556, doi:10.1175/JTECH-D-13-00206.1.

Chan, P. W., and A. M. Shao, 2007: Depiction of complex airflow near Hong Kong International Airport using a Doppler lidar with a two-dimensional wind retrieval technique. *Meteor. Z.,* **16,** 491–504, doi:10.1127/0941-2948/2007/0220.

Crespo, A., and J. Hernández, 1986: A numerical model of wind turbine wakes and wind farms. *Proceedings: EWEC '86; European Wind Energy Association Conference and Exhibition,* W. Palz and E. Sesto, Eds., Vol. 2, A. Raguzzi, Bookshop for Scientific Publications, 111–115.

——, ——, and S. Frandsen, 1999: Survey of modelling methods for wind turbine wakes and wind farms. *Wind Energy,* **2,** 1–24, doi:10.1002/(SICI)1099-1824(199901/03)2:1<1::AID-WE16>3.0.CO;2-7.

Delaunay, B., 1934: Sur la sphère vide. *Izv. Akad. Nauk SSSR Otd. Mat. Estestv. Nauk*, **7,** 793–800.

Elliott, D. L., and J. B. Cadogan, 1990: Effects of wind shear and turbulence on wind turbine power curves. *Proc. European Community Wind Energy Conf. and Exhibition,* Madrid, Spain, EWEA, 10–14.

Emeis, S., M. Harris, and R. Banta, 2007: Boundary-layer anemometry by optical remote sensing for wind energy applications. *Meteor. Z.,* **16,** 337–347, doi:10.1127/0941-2948/2007/0225.

Gottschall, J., and J. Peinke, 2008: How to improve the estimation of power curves for wind turbines. *Environ. Res. Lett.,* **3,** 015005, doi:10.1088/1748-9326/3/1/015005.

Högstrom, U., D. N. Asimakopoulos, H. Kambezidis, C. G. Helmis, and A. Smedman, 1988: A field study of the wake behind a 2 MW wind turbine. *Atmos. Environ.,* **22,** 803–820, doi:10.1016/0004-6981(88)90020-0.

Iungo, G. V., and F. Porté-Agel, 2013: Measurement procedures for characterization of wind turbine wakes with scanning Doppler wind LiDARs. *Adv. Sci. Res.,* **10,** 71–75, doi:10.5194/asr-10-71-2013.

——, F. Viola, S. Camarri, F. Porté-Agel, and F. Gallaire, 2013a: Linear stability analysis of wind turbine wakes performed on wind tunnel measurements. *J. Fluid Mech.,* **737,** 499–526, doi:10.1017/jfm.2013.569.

——, Y.-T. Wu, and F. Porté-Agel, 2013b: Field measurements of wind turbine wakes with lidars. *J. Atmos. Oceanic Technol.,* **30,** 274–287, doi:10.1175/JTECH-D-12-00051.1.

Kaimal, J. C., R. A. Eversole, D. H. Lenschow, B. B. Stankov, P. H. Kahn, and J. A. Businger, 1982: Spectral characteristics of the convective boundary layer over uneven terrain. *J. Atmos. Sci.,* **39,** 1098–1114.

Käsler, Y., S. Rahm, R. Simmet, and M. Kühn, 2010: Wake measurements of a multi-MW wind turbine with coherent long-range pulsed Doppler wind lidar. *J. Atmos. Oceanic Technol.,* **27,** 1529–1532, doi:10.1175/2010JTECHA1483.1.

Kongara, S., R. Calhoun, A. Choukulkar, and M. Boldi, 2012: Velocity retrieval for coherent Doppler lidar. *Int. J. Remote Sens.,* **33,** 3596–3613, doi:10.1080/01431161.2011.631948.

Larsen, S. E., S. E. Gryning, N. O. Jensen, H. E. Jørgensen, and J. Mann, 2007: Mean wind and turbulence in the atmospheric boundary layer above the surface layer. *Wind Energy: Proceedings of the Euromech Colloquium,* J. Peinke, P. Schaumann, and S. Barth, Eds., Springer, 21–25.

Lin, C., Q. Xia, and R. Calhoun, 2008: Retrieval of urban boundary layer structures from Doppler lidar data. Part II: Proper orthogonal decomposition. *J. Atmos. Sci.,* **65,** 21–42, doi:10.1175/2007JAS2329.1.

Luken, E., A. Talmon, and P. E. J. Vermeulen, 1986: Evaluation of two mathematical wind turbine wake models in various types of flow. TNO-MT Tech. Rep. 86-07, 24 pp.

Machefaux, E., N. Troldborg, G. C. Larsen, J. Mann, and H. A. Madsen, 2012: Experimental and numerical study of wake to wake interaction in wind farms. *Proc. European Wind Energy Conf. and Exhibition,* Copenhagen, Denmark, EWEA, 10 pp. [Available online at http://orbit.dtu.dk/en/publications/experimental-and-numerical-study-of-wake-to-wake-interaction-in-wind-farms(f10f9a8a-b95b-441f-acb5-fe0c38e22215).pdf?nofollow=true&rendering=long.]

Magnusson, M., and A.-S. Smedman, 1996: A practical method to estimate wind turbine wake characteristics from turbine data and routine wind measurements. *Wind Eng.,* **20,** 73–92.

——, and ——, 1999: Air flow behind wind turbines. *J. Wind Eng. Ind. Aerodyn.,* **80,** 169–189, doi:10.1016/S0167-6105(98)00126-3.

Monin, A. S., and A. M. Obukhov, 1954: Basic laws of turbulent mixing in the ground layer of the atmosphere. *Tr. Geofiz. Inst., Akad. Nauk SSSR,* **151,** 163–187.

Motta, M., R. J. Barthelmie, and P. Vølund, 2005: The influence of non-logarithmic wind speed profiles on potential power output at Danish offshore sites. *Wind Energy,* **8,** 219–236.

Newsom, R., D. Ligon, R. Calhoun, R. Heap, E. Cregan, and M. Pricevac, 2005: Retrieval of microscale wind and temperature fields from single- and dual-Doppler lidar data. *J. Appl. Meteor.,* **44,** 1324–1345, doi:10.1175/JAM2280.1.

Nieuwstadt, F. T. M., 1984: The turbulent structure of the stable, nocturnal boundary layer. *J. Atmos. Sci.,* **41,** 2202–2216, doi:10.1175/1520-0469(1984)041<2202:TTSOTS>2.0.CO;2.

Obukhov, A. M., 1971: Turbulence in an atmosphere with a non-uniform temperature. *Bound.-Layer Meteor.,* **2,** 7–29, doi:10.1007/BF00718085.

Panofsky, H. A., H. Tennekes, D. H. Lenschow, and J. C. Wyngaard, 1977: The characteristics of turbulent velocity components in the surface layer under convective conditions. *Bound.-Layer Meteor.,* **11,** 355–361, doi:10.1007/BF02186086.

Porté-Agel, F., Y.-T. Wu, H. Lu, and R. Conzemius, 2011: Large-eddy simulation of atmospheric boundary layer flow through wind turbines and wind farms. *J. Wind Eng. Ind. Aerodyn.,* **99,** 154–168, doi:10.1016/j.jweia.2011.01.011.

Rareshide, E., A. Tindal, C. Johnson, A. Graves, E. Simpson, J. Bleeg, T. Harris, and D. Schoborg, 2009: Effects of complex

wind regimes on turbine performance. *Proc. Windpower 2009,* Chicago, IL, AWEA, 15 pp.

Rhodes, M. E., and J. K. Lundquist, 2013: The effect of wind-turbine wakes on summertime US Midwest atmospheric wind profiles as observed with ground-based Doppler lidar. *Bound.-Layer Meteor.,* **149,** 85–103, doi:10.1007/s10546-013-9834-x.

Smalikho, I., V. Banakh, Y. Pichugina, W. Brewer, R. Banta, J. Lundquist, and N. Kelley, 2013: Lidar investigation of atmosphere effect on a wind turbine wake. *J. Atmos. Oceanic Technol.,* **30,** 2554–2570, doi:10.1175/JTECH-D-12-00108.1.

Smith, C. M., R. J. Barthelmie, and S. C. Pryor, 2013: *In situ* observations of the influence of a large onshore wind farm on near-surface temperature, turbulence intensity and wind speed profiles. *Environ. Res. Lett.,* **8,** 034006, doi:10.1088/1748-9326/8/3/034006.

Stull, R. B., 1988: *An Introduction to Boundary Layer Meteorology*. Atmospheric and Oceanographic Sciences Library, Vol. 13, Kluwer Academic, 670 pp.

Sumner, J., and C. Masson, 2006: Influence of atmospheric stability on wind turbine power performance curves. *J. Sol. Energy Eng.,* **128,** 531–538, doi:10.1115/1.2347714.

Takeuchi, K., 1961: On the structure of the turbulent field in the surface boundary layer. *J. Meteor. Soc. Japan,* **39,** 346–364.

Trujillo, J.-J., F. Bingöl, G. C. Larsen, J. Mann, and M. Kühn, 2011: Light detection and ranging measurements of wake dynamics. Part II: Two-dimensional scanning. *Wind Energy,* **14,** 61–75, doi:10.1002/we.402.

van der Berg, G. P., 2008: Wind turbine power and sound in relation to atmospheric stability. *Wind Energy,* **11,** 151–169, doi:10.1002/we.240.

Vermeer, L. J., J. N. Sørensen, and A. Crespo, 2003: Wind turbine wake aerodynamics. *Prog. Aerosp. Sci.,* **39,** 467–510, doi:10.1016/S0376-0421(03)00078-2.

Viola, F., G. V. Iungo, S. Camarri, F. Porté-Agel, and F. Gallaire, 2014: Prediction of the hub vortex instability in a wind turbine wake: Stability analysis with eddy-viscosity models calibrated on wind tunnel data. *J. Fluid Mech.,* **750,** R1, doi:10.1017/jfm.2014.263.

Wharton, S., and J. K. Lundquist, 2010: Atmospheric stability impacts on power curves of tall wind turbines—An analysis of a West Coast North American wind farm. LLNL Tech. Rep. LLNL-TR-424425, 73 pp. [Available online at https://e-reports-ext.llnl.gov/pdf/387609.pdf.]

——, and ——, 2012: Assessing atmospheric stability and its impacts on rotor-disk wind characteristics at an onshore wind farm. *Wind Energy,* **15,** 525–546, doi:10.1002/we.483.

Wiser, R., and M. Bollinger, 2012: 2011 wind technologies market report. Lawrence Berkeley National Laboratory Tech. Rep., 81 pp. [Available online at http://emp.lbl.gov/publications/2011-wind-technologies-market-report.]

Wu, Y.-T., and F. Porté-Agel, 2011: Large-eddy simulation of wind-turbine wakes: Evaluation of turbine parametrisations. *Bound.-Layer Meteor.,* **138,** 345–366, doi:10.1007/s10546-010-9569-x.

——, and ——, 2012: Atmospheric turbulence effects on wind-turbine wakes: An LES study. *Energies,* **5,** 5340–5362, doi:10.3390/en5125340.

Xia, Q., C. Lin, R. Calhoun, and R. Newsom, 2008: Retrieval of urban boundary layer structures from Doppler lidar data. Part I: Accuracy assessment. *J. Atmos. Sci.,* **65,** 3–20, doi:10.1175/2007JAS2328.1.

Zhang, W., C. D. Markfort, and F. Porté-Agel, 2013: Wind-turbine wakes in a convective boundary layer: A wind-tunnel study. *Bound.-Layer Meteor.,* **146,** 161–179, doi:10.1007/s10546-012-9751-4.

Zhou, L., Y. Tian, S. Baidya Roy, C. Thorncroft, L. F. Bosart, and Y. Hu, 2012: Impacts of wind farms on land surface temperature. *Nat. Climate Change,* **2,** 539–543, doi:10.1038/nclimate1505.